p-Poisson surface reconstruction in curl-free flow from point clouds

Yesom Park[1]*, Taekyung Lee[2]*, Jooyoung Hahn[3], Myungjoo Kang[1]
[1] Department of Mathematical Sciences, Seoul National University
[2] Interdisciplinary Program in Artificial Intelligence, Seoul National University
[3] Department of Mathematics and Descriptive Geometry,
Slovak University of Technology in Bratislava
{yeisom, dlxorud1231, mkang}@snu.ac.kr
jooyoung.hahn@stuba.sk

Abstract

The aim of this paper is the reconstruction of a smooth surface from an unorganized point cloud sampled by a closed surface, with the preservation of geometric shapes, without any further information other than the point cloud. Implicit neural representations (INRs) have recently emerged as a promising approach to surface reconstruction. However, the reconstruction quality of existing methods relies on ground truth implicit function values or surface normal vectors. In this paper, we show that proper supervision of partial differential equations and fundamental properties of differential vector fields are sufficient to robustly reconstruct high-quality surfaces. We cast the p-Poisson equation to learn a signed distance function (SDF) and the reconstructed surface is implicitly represented by the zero-level set of the SDF. For efficient training, we develop a variable splitting structure by introducing a gradient of the SDF as an auxiliary variable and impose the p-Poisson equation directly on the auxiliary variable as a hard constraint. Based on the curl-free property of the gradient field, we impose a curl-free constraint on the auxiliary variable, which leads to a more faithful reconstruction. Experiments on standard benchmark datasets show that the proposed INR provides a superior and robust reconstruction. The code is available at `https://github.com/Yebbi/PINC`.

1 Introduction

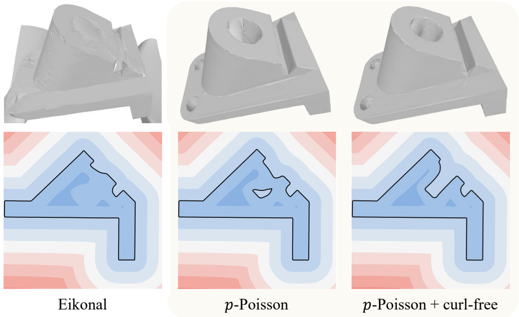

Figure 1: Comparison of reconstruction using an eikonal equation (9), the p-Poisson equation (8), and the proposed p-Poisson equation with the curl-free condition (11).

Surface reconstruction from an unorganized point cloud has been extensively studied for more than two decades [10, 29, 40, 9, 62] due to its many downstream applications in computer vision and computer graphics[8, 16, 62, 58]. Classical point cloud or mesh-based representations are efficient but they do not guarantee a watertight surface and are usually limited to fixed geometries. Implicit function-based representations of the surface [28, 64, 43, 14] as a level set $\mathcal{S} = \left\{\mathbf{x} \in \mathbb{R}^3 \mid u\left(\mathbf{x}\right) = c\right\}$ of a continuous implicit function $u : \mathbb{R}^3 \to \mathbb{R}$, such as signed distance functions (SDFs) or occupancy functions, have received considerable attention for providing watertight results and great flexibility

[*] Equal contribution authors. Correspondence to: <mkang@snu.ac.kr>.

37th Conference on Neural Information Processing Systems (NeurIPS 2023).

in representing different topologies. In recent years, with the rise of deep learning, a stream of work called *implicit neural representations* (INRs) [2, 44, 16, 61, 19, 55, 53, 50] has revisited them by parameterizing the implicit function u with neural networks. INRs have shown promising results by offering efficient training and expressive surface reconstruction.

Early INRs [44, 42, 16] treat the points-to-surface problem as a supervised regression problem with ground-truth distance values, which are difficult to use in many situations. To overcome this limitation, some research efforts have used partial differential equations (PDEs), typically the eikonal equation, as a means to relax the 3D supervision [23, 37, 48]. While these efforts have been successful in reconstructing various geometries, they encounter an issue of non-unique solutions in the eikonal equation and rely heavily on the oriented normal vector at each point. They often fail to capture fine details or reconstruct plausible surfaces without normal vectors. A raw point cloud usually lacks normal vectors or numerically estimated normal vectors [1, 18] contain approximation errors. Moreover, the prior works are vulnerable to noisy observations and outliers.

The goal of this work is to propose an implicit representation of surfaces that not only provides smooth reconstruction but also recovers high-frequency features only from a raw point cloud. To this end, we provide a novel approach that expresses an approximated SDF as the unique solution to the p-Poisson equation. In contrast to previous studies that only describe the SDF as a network, we define the gradient of the SDF as an auxiliary variable, motivated by variable splitting methods [47, 60, 22, 12] in the optimization literature. We then parameterize the auxiliary output to automatically satisfy the p-Poisson equation by reformulating the equation in a divergence-free form. The divergence-free splitting representation contributes to efficient training by avoiding deeply nested gradient chains and allows the use of sufficiently large p, which permits an accurate approximation of the SDF. In addition, we impose a curl-free constraint [25] because the auxiliary variable should be learned as a conservative vector field which has vanishing curl. The curl-free constraint serves to achieve a faithful reconstruction. We carefully evaluate the proposed model on widely used benchmarks and robustness to noise. The results demonstrate the superiority of our model without a priori knowledge of the surface normal at the data points.

2 Background and related works

Implicit neural representations In recent years, implicit neural representations (INRs) [41, 16, 3, 55, 54], which define a surface as zero level-sets of neural networks, have been extensively studied. Early work requires the ground-truth signed implicit function [44, 16, 41], which is difficult to obtain in real-world scenarios. Considerable research [3, 4] is devoted to removing 3D supervision and relaxing it with a ground truth normal vector at each point. In particular, several efforts use PDEs to remove supervision and learn implicit functions only from raw point clouds. Recently, IGR [23] revisits a conventional numerical approach [14] that accesses the SDF by incorporating the eikonal equation into a variational problem by using modern computational tools of deep learning. Without the normal vector, however, IGR misses fine details. To alleviate this problem, FFN [56] and SIREN [55] put the high frequencies directly into the network. Other approaches exploit additional loss terms to regulate the divergence [6] or the Hessian [63]. The vanishing viscosity method, which perturbs the eikonal equation with a small diffusion term, is also considered [37, 49] to mitigate the drawback that the eikonal loss has unreliable minima. The classical Poisson reconstruction [31], which recovers the implicit function by integration over the normal vector field, has also been revisited to accelerate the model inference time [48], but supervision of the normal vector field is required. Neural-Pull [39] constructs a new loss function by borrowing the geometrical property that the SDF and its gradient define the shortest path to the surface.

p-Poisson equation The SDF is described by a solution of various PDEs. The existing work [23, 55, 6] uses the eikonal equation, whose viscosity solution describes the SDF. However, the use of the residual of the eikonal equation as a loss function raises concerns about the convergence to the SDF due to non-unique solutions of the eikonal equation. Recent works [55, 6] utilize the notion of vanishing viscosity to circumvent the issue of non-unique solutions. In this paper, we use the p-Poisson equation to approximate the SDF, which is a nonlinear generalization of the Poisson equation ($p = 2$):

$$\begin{cases} -\triangle_p u = -\nabla \cdot \left(\|\nabla u\|^{p-2} \nabla u \right) = 1 \text{ in } \Omega \\ u = 0 \text{ on } \Gamma, \end{cases} \tag{1}$$

where $p \geq 2$, the computation domain $\Omega \subset \mathbb{R}^3$ is bounded, and Γ is embedded in Ω.

The main advantage of using the p-Poisson equation is that the solution to (1) is unique in Sobolev space $W^{1,p}(\Omega)$ [36]. The unique solution with $p \geq 2$ brings a viscosity solution of the eikonal equation in the limit $p \to \infty$, which is the SDF, and it eventually prevents finding non-viscosity solutions of the eikonal equation; see a further discussion with an example in Appendix C.1. Moreover, in contrast to the eikonal equation, it is possible to describe a solution of (1) as a variational problem and compute an accurate approximation [5, 20]:

$$\min_u \int_\Omega \frac{\|\nabla u\|^p}{p} d\mathbf{x} - \int_\Omega u d\mathbf{x}. \tag{2}$$

As $p \to \infty$, it has been shown [11, 30] that the solution u of (1) converges to the SDF whose zero level set is Γ. As a result, increasing p gives a better approximation of the SDF, which is definitely helpful for surface reconstruction. However, it is still difficult to use a fairly large p in numerical computations and in this paper we will explain one of the possible solutions to the mentioned problem.

3 Method

In this section, we propose a p-**P**oisson equation based **I**mplicit **N**eural representation with **C**url-free constraint (**PINC**). From an unorganized point cloud $\mathcal{X} = \{\mathbf{x}_i : i = 1, 2, \dots, N\}$ sampled by a closed surface Γ, a SDF $u : \mathbb{R}^3 \to \mathbb{R}$ whose zero level set is the surface $\Gamma = \left\{\mathbf{x} \in \mathbb{R}^3 \mid u(\mathbf{x}) = 0\right\}$ is reconstructed by the proposed INR. There are two key elements in the proposed method: First, using a variable-splitting representation [45] of the network, an auxiliary output is used to learn the gradient of the SDF that satisfies the p-Poisson equation (1). Second, a curl-free constraint is enforced on an auxiliary variable to ensure that the differentiable vector identity is satisfied.

3.1 p-Poisson equation

A loss function in the physics-informed framework [51] of the existing INRs for the p-Poisson equation (1) can be directly written:

$$\min_u \int_\Gamma |u| \, d\mathbf{x} + \lambda_0 \int_\Omega \left| \nabla \cdot \left(\|\nabla u\|^{p-2} \nabla u \right) + 1 \right| d\mathbf{x}, \tag{3}$$

where $\lambda_0 > 0$ is a regularization constant. To reduce the learning complexity of the second integrand, we propose an augmented network structure that separately parameterizes the gradient of the SDF as an auxiliary variable that satisfies the p-Poisson equation (1).

Variable-splitting strategy Unlike existing studies [23, 37, 6] that use neural networks with only one output u for the SDF, we introduce a separate auxiliary network output G for the gradient of the SDF; see that the same principle is used in [45]. In the optimization literature, it is called the variable splitting method [47, 60, 22, 12] and it has the advantage of decomposing a complex minimization into a sequence of relatively simple sub-problems. With the auxiliary variable $G = \nabla u$ and the penalty method [13], the variational problem (3) is converted into an unconstrained problem:

$$\min_{u,G} \int_\Gamma |u| \, d\mathbf{x} + \lambda_0 \int_\Omega \left| \nabla \cdot \left(\|G\|^{p-2} G \right) + 1 \right| d\mathbf{x} + \lambda_1 \int_\Omega \|\nabla u - G\|^2 \, d\mathbf{x}, \tag{4}$$

where $\lambda_1 > 0$ is a penalty parameter representing the relative importance of the loss terms.

p-Poisson as a hard constraint Looking more closely at the minimization (4), if G is already a gradient to satisfy (1), then the second term in (4) is no longer needed and it brings the simplicity of one less parameter. Now, for a function $F : \Omega \to \mathbb{R}^3$ such that $\nabla \cdot F = 1$, for example $F(\mathbf{x}) = \frac{1}{3}\mathbf{x}$, the p-Poisson equation (1) is reformulated by the divergence-free form:

$$\nabla \cdot \left(\|\nabla u\|^{p-2} \nabla u + F \right) = 0. \tag{5}$$

Then, there exists a vector potential $\Psi : \mathbb{R}^3 \to \mathbb{R}^3$ satisfying

$$\|G\|^{p-2} G + F = \nabla \times \Psi, \tag{6}$$

where $G = \nabla u$. Note that a similar idea is used in the neural conservation law [52] to construct a divergence-free vector field built on the Helmholtz decomposition [33, 57]. From the condition (6), we have $\|G\|^{p-1} = \|\nabla \times \Psi - F\|$ and G is parallel to $\nabla \times \Psi - F$, then the auxiliary output G is explicitly written:

$$G = \frac{\nabla \times \Psi - F}{\|\nabla \times \Psi - F\|^{\frac{p-2}{p-1}}}. \tag{7}$$

This confirms that the minimization problem (4) does not require finding G directly, but rather that it can be obtained from the vector potential Ψ. Therefore, the second loss term in (4) can be eliminated by approximating the potential function Ψ by a neural network and defining the auxiliary output G as a hard constraint (7). To sum up, we use a loss function of the form

$$\mathcal{L}_{p\text{-Poisson}} = \int_{\Gamma} |u| \, d\mathbf{x} + \lambda_1 \int_{\Omega} \|\nabla u - G\|^2 \, d\mathbf{x}, \tag{8}$$

where G is obtained by (7), the first term is responsible for imposing the boundary condition of (1), and the second term enforces the constraint $G = \nabla u$ between primary and auxiliary outputs. It is worth mentioning that G in (7) is designed to exactly satisfy the p-Poisson equation (1).

An advantage of the proposed loss function (8) and the hard constraint (7) is that (1) can be solved for sufficiently large p, which is critical to make a better approximation of the SDF. It is not straightforward in (3) or (4) because the numeric value of $(p-2)$-power with a large p easily exceeds the limit of floating precision. On the other hand, in (7) we use $(p-2)/(p-1)$-power, which allows stable computation even when p becomes arbitrarily large. The surface reconstruction with varying p in Figure 7 shows that using a large enough p is crucial to get a good reconstruction. As the p increases, the reconstruction gets closer and closer to the point cloud. Furthermore, it is worth noting that the proposed representation expresses the second-order PDE (1) with first-order derivatives only. By reducing the order of the derivatives, the computational graph is simplified than (3) or (4).

Note that one can think of an approach to directly solve the eikonal equation $\|\nabla u\| = 1$ with an auxiliary variable $H = \nabla u$ as an output of the neural network:

$$\min_{u, \|H\|=1} \int_{\Gamma} |u| \, d\mathbf{x} + \eta \int_{\Omega} \|\nabla u - H\|^2 \, d\mathbf{x}, \tag{9}$$

where $\eta > 0$. The above loss function may produce a non-unique solution of the eikonal equation, which causes numerical instability and undesirable estimation of the surface reconstruction; see Figure 1. To alleviate such an issue, the vanishing viscosity method is used in [37, 49] to approximate the SDF by u_σ as $\sigma \to 0$, a solution of $-\sigma \triangle u_\sigma + \operatorname{sign}(u_\sigma)(|\nabla u_\sigma| - 1) = 0$. However, the results are dependent on the hyper-parameter $\sigma > 0$ related to the resolution of the discretized computational domain and the order of the numerical scheme [17, 24].

3.2 Curl-free constraint

In the penalty method, we have to compute more strictly to ensure that $G = \nabla u$ by using progressively larger values of λ_1 in (8), but in practice we cannot make the value of λ_1 infinitely large. Now, we can think of yet another condition for enforcing the constraint $G = \nabla u$ from a differential vector identity which says a conservative vector field is curl-free:

$$\nabla \times G = 0 \iff G = \nabla u \tag{10}$$

for some scalar potential function u. While it may seem straightforward, adding a penalty term $\int_\Omega \|\nabla \times G\|^2 \, d\mathbf{x}$ at the top of (8) is fraught with problems. Since G is calculated by using a curl operation (7), the mentioned penalty term makes a long and complex computational graph. In addition, it has been reported that such loss functions, which include high-order derivatives computed by automatic differentiation, induce a loss landscape that is difficult to optimize [34, 59]. In order to relax the mentioned issue, we augment another auxiliary variable $\tilde{G}$, where $G = \tilde{G}$ and $\nabla \times \tilde{G} = 0$ are constrained.

By incorporating the new auxiliary variable $\tilde{G}$ and its curl-free constraint, we have the following loss function:

$$\mathcal{L}_{\text{PINC}} = \mathcal{L}_{p\text{-Poisson}} + \lambda_2 \int_{\Omega} \left\| G - \tilde{G} \right\|^2 d\mathbf{x} + \lambda_3 \int_{\Omega} \left\| \nabla \times \tilde{G} \right\|^2 d\mathbf{x}. \tag{11}$$

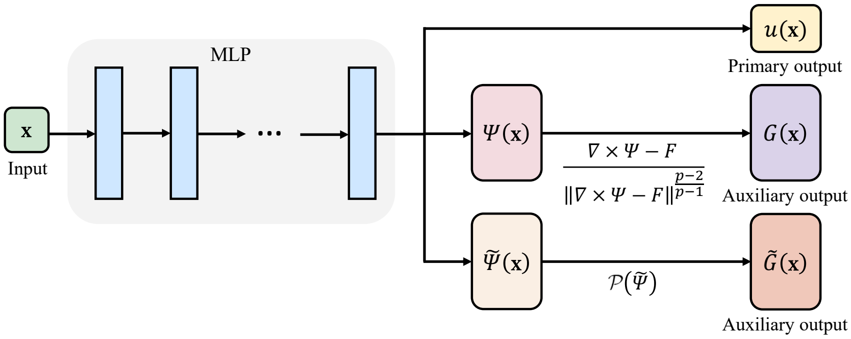
MLP
x
Input
$u(\mathbf{x})$
Primary output
$\Psi(\mathbf{x})$
$\frac{\nabla \times \Psi - F}{\|\nabla \times \Psi - F\|^{\frac{p-2}{p-1}}}$
$G(\mathbf{x})$
Auxiliary output
$\tilde{\Psi}(\mathbf{x})$
$\mathcal{P}(\tilde{\Psi})$
$\tilde{G}(\mathbf{x})$
Auxiliary output

Figure 2: The visualization of the augmented network structure with two auxiliary variables.

Note that the optimal $\tilde{G}$ should have a unit norm according to the eikonal equation. To facilitate training, we relax this nonconvex equality condition into a convex constraint $\| \tilde{G} \| \leq 1$. To this end, we parameterize the second network auxiliary output $\tilde{\Psi}$ and define $\tilde{G}$ by

$$\tilde{G} = \mathcal{P}\left(\tilde{\Psi}\right) := \frac{\tilde{\Psi}}{\max\left\{1, \| \tilde{\Psi} \|\right\}}, \tag{12}$$

where $\mathcal{P}$ is the projection operator to the three-dimensional unit ball. Appendix A provides further discussion on the importance of the curl-free term to learn a conservative vector field.

Figure 2 illustrates the proposed network architecture. The primary and the auxiliary variables are trained in a single network, instead of being trained separately in individual networks. The number of network parameters remains almost the same since only the output dimension of the last layer is increased by six, while all hidden layers are shared.

3.3 Proposed loss function

In the case of a real point cloud to estimate a closed surface by range scanners, it is inevitable to have occluded parts of the surface where the surface has a concave part depending on possible angles of the measurement [35]. It ends up having relatively large holes in the measured point cloud. Since there are no points in the middle of the hole, it is necessary to have a certain criterion for how to fill in the hole. In order to focus to check the quality of $\mathcal{L}_{\text{PINC}}$ (11) in this paper, we choose a simple rule to minimize the area of zero level set of u:

$$\mathcal{L}_{\text{total}} = \mathcal{L}_{\text{PINC}} + \lambda_4 \int_{\Omega} \delta_\epsilon\left(u\right) \|\nabla u\| \, d\mathbf{x}, \tag{13}$$

where $\lambda_4 > 0$ and $\delta_\epsilon(x) = 1 - \tanh^2\left(\frac{x}{\epsilon}\right)$ is a smeared Dirac delta function with $\epsilon > 0$. The minimization of the area is used in [21, 49] and the advanced models [15, 27, 63] on missing parts of the point cloud to provide better performance of the reconstruction.

4 Experimental results

In this section, we evaluate the performance of the proposed model to reconstruct 3D surfaces from point clouds. We study the following questions: **(i)** How does the proposed model perform compared to existing INRs? **(ii)** Is it stable from noise? **(iii)** What is the role of the parts that make up the model and the loss? Each is elaborated in order in the following sections.

Implementation As in previous studies [44, 23, 37], we use an 8-layer network with 512 neurons and a skip connection to the middle layer, but only the output dimension of the last layer is increased by six due to the auxiliary variables. For (13), we empirically set the loss coefficients to $\lambda_1 = 0.1$, $\lambda_2 = 0.0001$. $\lambda_3 = 0.0005$, and $\lambda_4 = 0.1$ and use $p = \infty$ in (7) for numerical simplicity. We implement all numerical experiments on a single NVIDIA RTX 3090 GPU. In all experiments, we use the Adam optimizer [32] with learning rate 10^{-3} decayed by 0.99 every 2000 iterations.

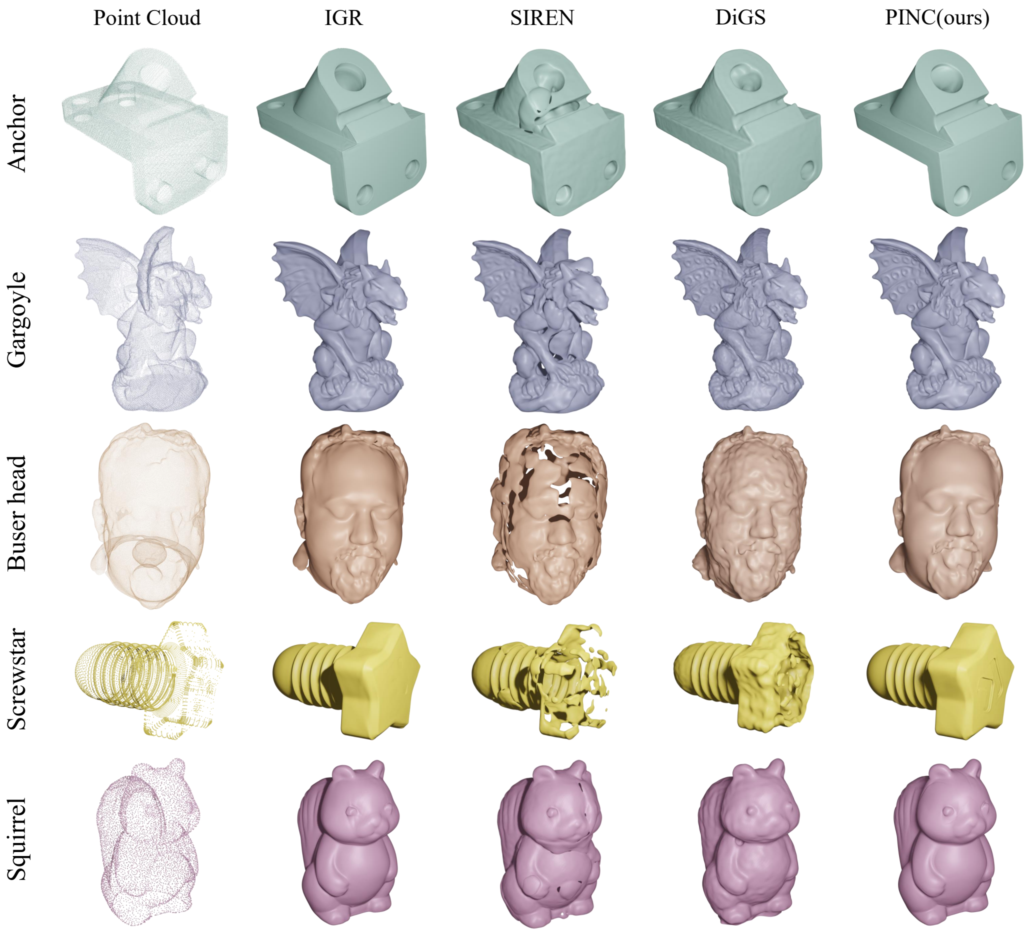

Figure 3: 3D Reconstruction results for SRB and Thingi10K datasets.

Datasets We leverage two widely used benchmark datasets to evaluate the proposed model for surface reconstruction: Surface Reconstruction Benchmark (SRB) [7] and Thingi10K [65]. The geometries in the mentioned datasets are challenging because of their complex topologies and incomplete observations. Following the prior works, we adopt five objects per dataset. We normalize the input data to center at zero and have a maximum norm of one.

Baselines We compare the proposed model with the following baselines: IGR [23], SIREN [55], SAL [3], PHASE [37], and DiGS [6]. All models are evaluated from only raw point cloud data without surface normal vectors. A comparison with models that leverage surface normals as supervision is included in Appendix C.

Metrics To estimate the quantitative accuracy of the reconstructed surface, we measure Chamfer (d_C) and Hausdorff (d_H) distances between the ground-truth point clouds and the reconstructed surfaces. Moreover, we report one-sided distances $d_{\overrightarrow{C}}$ and $d_{\overrightarrow{H}}$ between the noisy data and the reconstructed surfaces. Please see Appendix B.2 for precise definitions.

4.1 Surface reconstruction

We validate the performance of the proposed PINC (13) in surface reconstruction in comparison to other INR baselines. For a fair comparison, we consider the baseline models that were trained without a normal prior. Table 1 summarizes the numerical comparison on SRB in terms of metrics. We report the results of baselines from [37, 49, 6]. The results show that the reconstruction quality obtained is on par with the leading INRs, and we achieved state-or-the-art performance for Chamfer distances.

Table 1: Results on surface reconstruction of SRB.

	Anchor				Daratech				DC				Gargoyle				Loard Quas			
	GT		Scans		GT		Scans		GT		Scans		GT		Scans		GT		Scans	
Model	d_C	d_H	$d_{\vec{C}}$	$d_{\vec{H}}$	d_C	d_H	$d_{\vec{C}}$	$d_{\vec{H}}$	d_C	d_H	$d_{\vec{C}}$	$d_{\vec{H}}$	d_C	d_H	$d_{\vec{C}}$	$d_{\vec{H}}$	d_C	d_H	$d_{\vec{C}}$	$d_{\vec{H}}$
IGR	0.45	7.45	0.17	4.55	4.9	42.15	0.7	3.68	0.63	10.35	0.14	3.44	0.77	17.46	0.18	2.04	0.16	4.22	0.08	1.14
SIREN	0.72	10.98	0.11	1.27	0.21	4.37	0.09	1.78	0.34	6.27	0.06	**2.71**	0.46	7.76	0.08	**0.68**	0.35	8.96	0.06	**0.65**
SAL	0.42	7.21	0.17	4.67	0.62	13.21	0.11	2.15	0.18	3.06	0.08	2.82	0.45	9.74	0.21	3.84	0.13	414	0.07	4.04
PHASE	**0.29**	7.43	**0.09**	1.49	0.35	7.24	**0.08**	**1.21**	0.19	4.65	0.05	2.78	0.17	4.79	0.07	1.58	0.11	**0.71**	0.05	0.74
DiGS	**0.29**	**7.19**	0.11	1.17	**0.20**	**3.72**	0.09	1.80	0.15	**1.70**	0.07	2.75	0.17	**4.10**	0.09	0.92	0.12	0.91	0.06	0.70
PINC	**0.29**	7.54	**0.09**	1.20	0.37	7.24	0.11	1.88	**0.14**	2.56	**0.04**	2.73	**0.16**	4.78	**0.05**	0.80	**0.10**	0.92	**0.04**	0.67

Table 2: Results on surface reconstruction of Thingi10K.

	Squirrel		Buser head		Screwstar		Frogrock		Pumpkin	
Model	d_C	d_H	d_C	d_H	d_C	d_H	d_C	d_H	d_C	d_H
IGR	0.36	11.97	0.38	5.95	0.18	3.02	0.48	12.05	0.11	**1.13**
SIREN	0.47	**5.66**	0.43	**4.81**	0.27	4.98	0.78	14.75	0.46	5.03
DiGS	0.50	12.45	0.39	10.64	0.26	6.33	0.45	**10.50**	0.32	8.03
PINC	**0.35**	11.55	**0.37**	6.19	**0.17**	**3.00**	**0.43**	11.06	**0.10**	1.90

We further verify the accuracy of the reconstructed surface for the Thingi10K dataset by measuring the metrics. For Thingi10K, we reproduce the results of IGR, SIREN, and DiGS without normal vectors using the official codes. Results on Thingi10K presented in Table 2 show the proposed method achieves superior performance compared to existing approaches. PINC achieves similar or better metric values on all objects.

The qualitative results are presented in Figure 3. SIREN, which imposes high-frequency features to the model by using a sine periodic function as activation, restores a somewhat torn surface. Similarly, DiGS restores rough and rogged surfaces, for example, the human face and squirrel body are not smooth and are rendered unevenly. On the other hand, IGR provides smooth surfaces but tends to over-smooth details such as the gargoyle's wings and detail on the star-shaped bolt head of screwstar. The results confirm that the proposed PINC (13) adopts both of these advantages: PINC represents a smooth and detailed surface. More results can be found in the Appendix C.

4.2 Reconstruction from noisy data

In this section, we analyze whether the proposed PINC (13) produces robust results to the presence of noise in the input point data. In many situations, the samples obtained by the scanning process contain a lot of noise and inaccurate surface normals are estimated from these noisy samples. Therefore, it is an important task to perform accurate reconstruction using only noisy data without normal vectors. To investigate the robustness to noise, we perturb the data with additive Gaussian noise with mean zero and two standard deviations 0.005 and 0.01.

We quantify the ability of the proposed model to handle noise in the input points. The qualitative results are shown in Figure 4. Compared to existing methods, the results demonstrate superior resilience of the proposed model with respect to noise corruption in the input samples. We can observe that SIREN and DiGS restore broken surfaces that appear to be small grains as the noise level increases. On the other hand, the proposed model produces a relatively smooth reconstruction. Results show that PINC is less sensitive to noise than others.

4.3 Ablation studies

This section is devoted to ablation analyses which show that each part of the proposed loss function $\mathcal{L}_{\text{total}}$ in conjunction with the divergence-free splitting architecture plays an important role in high-quality reconstruction.

Effect of curl-free constraint We first study the effect of the curl-free constraint on reconstructing high fidelity surfaces. To investigate the effectiveness of the proposed curl-free constraint, we compare the performance of PINC without the curl-free loss term, i.e., the model trained with the loss function $\mathcal{L}_{p\text{-Poisson}}$ (8). The results on the SRB dataset are reported in Table 3 and Figure 5. Figure 5

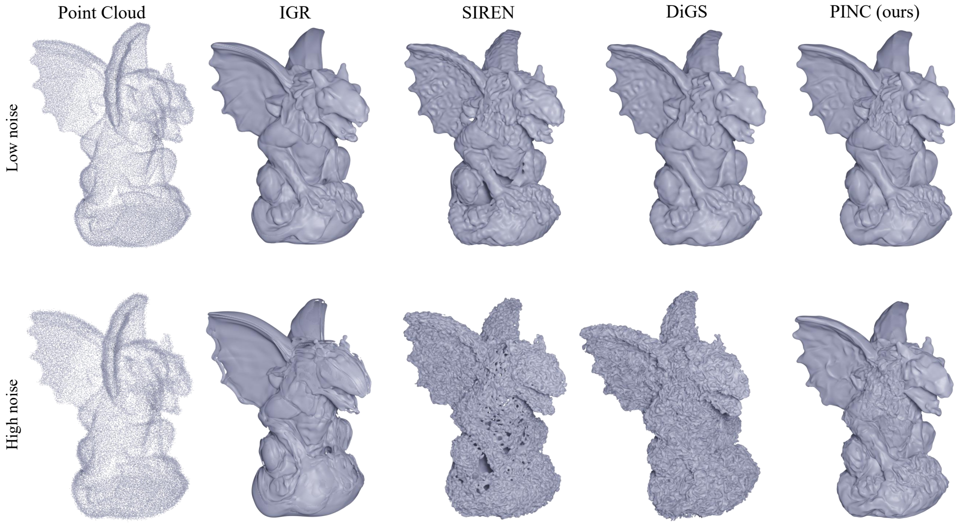

Figure 4: Reconstruction results from noisy observations. Two levels of additive Gaussian noise with standard deviations $\sigma = 0.005$ (low) and 0.01 (high) are considered.

shows that the variable splitting method, which satisfies the p-Poisson equation as a hard constraint (without the curl-free condition), recovers a fairly decent surface, but it generates oversmoothed surfaces and details are lost. However, as we can see from the qualitative result reconstructed with the curl-free constraint, this constraint allows us to capture the details that PINC without the curl-free condition cannot recover. The metric values presented in Table 3 also provide clear evidence of the need for the curl-free term. To further examine the necessity of another auxiliary variable $\tilde{G}$, we conduct an additional experiment by applying the curl-free loss term directly on G without the use of $\tilde{G}$. The results are presented in the second row of the Table 3. The results indicate that taking curl on G, which is constructed by taking curl on Ψ in (7), leads to a suboptimal reconstruction. This is likely due to a challenging optimization landscape that is difficult to optimize as a result of consecutive automatic differentiation [59]. The results provide numerical evidences of the necessity of introducing $\tilde{G}$.

Table 3: Quantitative results on the ablation study of the curl-free term.

	GT		Scans	
Model	d_C	d_H	$d_{\vec{C}}$	$d_{\vec{H}}$
wo/ curl free	0.20	4.96	0.12	2.98
w/ curl free on G	4.17	52.26	0.48	6.03
w/ curl free on $\tilde{G}$	0.16	4.78	0.05	0.80

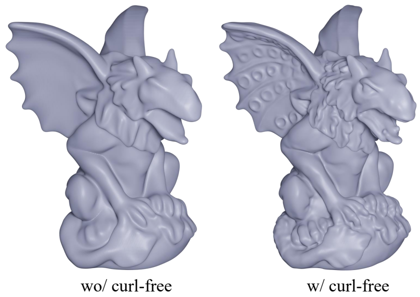

Figure 5: Comparison of surface reconstruction without (left) and with (right) curl-free constraint.

Effect of minimal area criterion We study the effect of the minimal area criterion suggested in Section 3.3. In real scenarios, there are defected regions where the surface has not been measured. To fill this part of the hole, the minimum surface area is considered. Figure 6 clearly shows this effect. Some parts in the daratech of SRB have a hole in the back. Probably because of this hole, parts that are not manifolds are spread out as manifolds as shown in the left figure without considering the minimal area. However, we can see that adding a minimal area loss term alleviates this problem. We would like to note that, except for daratech, we did not encounter this problem because other data are point clouds sampled from a closed surface and also are not related to hole filling. Indeed, we empirically observe that the results are quite similar with and without the minimal area term for all data other than daratech.

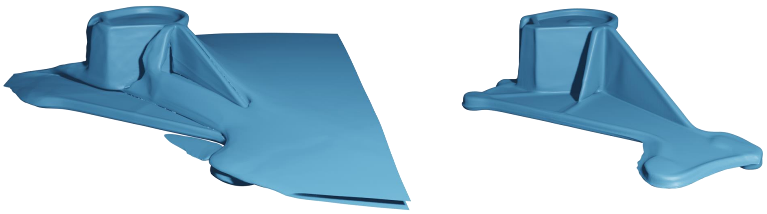

(a) wo/ area loss

(b) w/ area loss

Figure 6: Comparison of surface recovery without (a) and with (b) minimum area criterion.

Effect of large p The p-Poisson equation (1) draws the SDF as p becomes infinitely large. Therefore, it is natural to think that it would be good to use a large p. Here, we conducted experiments on the effect of p. We define G with various $p = 2, 10,$ and 100 and learn the SDF with it. Figure 7 shows surfaces that were recovered from the Gargoyle data in the SRB with different p values. When p is as small as 2, it is obvious that it is difficult to reconstruct a compact surface from points. When p is 10, a much better surface is constructed than that of $p = 2$, but the by-products still remain on the small holes. Furthermore, a large value of $p = 100$ provides a quite proper reconstruction. This experimental result demonstrates that a more accurate approximation can be obtained by the use of a large p, which is consistent with the theory. This once again highlights the advantage of the variable splitting method we have proposed, which allows an arbitrarily large p to be used. This highlights the advantage of the variable splitting method (7) we have proposed in Section 3.1, which allows an arbitrarily large p to be used. Note that the previous approaches have not been able to use large p because the numeric value of p-power easily exceeds the limit of floating precision. On the other hand, the proposed method is amenable to large p and hence the reconstruction becomes closer to the point cloud.

5 Conclusion and limitations

We presented a p-Poisson equation-based shape representation learning, termed PINC, that reconstructs high-fidelity surfaces using only the locations of given points. We introduced the gradient of the SDF as an auxiliary network output and incorporated the p-Poisson equation into the auxiliary variable as a hard constraint. The curl-free constraint was also used to provide a more accurate representation. Furthermore, the minimal surface area regularization was considered to provide a compact surface and overcome the ill-posedness of the surface reconstruction problem caused by unobserved points. The proposed PINC successively achieved a faithful surface with intricate details and was robust to noisy observations.

The minimization of the surface area is used to reconstruct missing parts of points under the assumption that a point cloud is measured by a closed surface. Regarding the hole-filling strategy, it still needs further discussion and investigation of various constraints such as mean curvature or total variation of the gradient. At present, the proposed PDE-based framework is limited to closed surfaces and is inadequate to reconstruct open surfaces. We leave the development to open surface reconstruction as future work. Establishing a neural network initialization that favors the auxiliary gradient of the SDF would be an interesting venue. Furthermore, the computational cost of convergence would differ when using and not using auxiliary variables. Analyzing the convergence speed or computational cost of utilizing auxiliary variables versus not utilizing them is a worthwhile direction for future research.

6 Societal Impacts

The proposed PINC allows high-quality representation of 3D shapes only from raw unoriented 3D point cloud. It has many potential downstream applications, including product design, security, medical imaging, robotics, and the film industry. We are aware that accurate 3D surface reconstruction

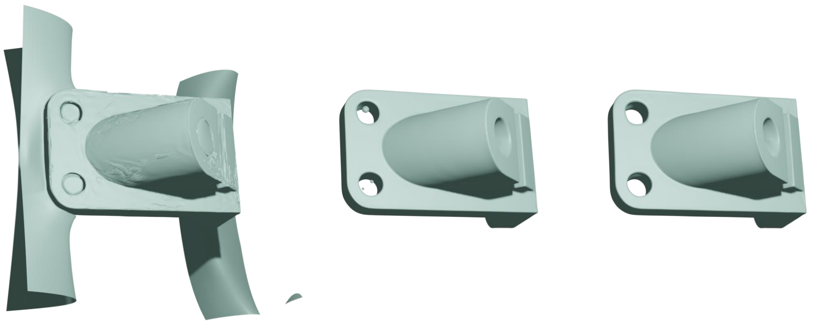

(a) $p = 2$ (b) $p = 10$ (c) $p = 100$

Figure 7: Surface reconstruction of anchor data with various p. The results show the importance of using a sufficiently large p for an accurate approximation.

can be used in malicious environments such as unauthorized reproduction of machines without consent and digital impersonation. However, it is not a work to develop a technique to go to abuse, and we hope and encourage users of the proposed model to concenter on the positive impact of this work.

7 Acknowledgements

This work was supported by the NRF grant [2012R1A2C3010887] and the MSIT/IITP ([1711117093], [2021-0-00077], [No. 2021-0-01343, Artificial Intelligence Graduate School Program(SNU)]). Also, this project has received funding from the European Union's Horizon 2020 research and innovation programme under the Marie Skłodowska-Curie grant agreement No. 945478.

References

[1] Nina Amenta and Marshall Bern. Surface reconstruction by Voronoi filtering. In *Proceedings of the Fourteenth Annual Symposium on Computational Geometry*, pages 39–48, 1998.

[2] Matan Atzmon, Niv Haim, Lior Yariv, Ofer Israelov, Haggai Maron, and Yaron Lipman. Controlling neural level sets. *Advances in Neural Information Processing Systems*, 32, 2019.

[3] Matan Atzmon and Yaron Lipman. SAL: Sign agnostic learning of shapes from raw data. In *Proceedings of the IEEE/CVF Conference on Computer Vision and Pattern Recognition*, pages 2565–2574, 2020.

[4] Matan Atzmon and Yaron Lipman. SALD: Sign agnostic learning with derivatives. *arXiv preprint arXiv:2006.05400*, 2020.

[5] Alexander G. Belyaev and Pierre-Alain Fayolle. On variational and PDE-based distance function approximations. In *Computer Graphics Forum*, volume 34, pages 104–118. Wiley Online Library, 2015.

[6] Yizhak Ben-Shabat, Chamin Hewa Koneputugodage, and Stephen Gould. DiGS: Divergence guided shape implicit neural representation for unoriented point clouds. In *2022 IEEE/CVF Conference on Computer Vision and Pattern Recognition (CVPR)*, pages 19301–19310, 2022.

[7] Matthew Berger, Joshua A Levine, Luis Gustavo Nonato, Gabriel Taubin, and Claudio T Silva. A benchmark for surface reconstruction. *ACM Transactions on Graphics (TOG)*, 32(2):1–17, 2013.

[8] Matthew Berger, Andrea Tagliasacchi, Lee M. Seversky, Pierre Alliez, Gael Guennebaud, Joshua A Levine, Andrei Sharf, and Claudio T Silva. A survey of surface reconstruction from point clouds. In *Computer graphics forum*, volume 36, pages 301–329. Wiley Online Library, 2017.

[9] Matthew Berger, Andrea Tagliasacchi, Lee M. Seversky, Pierre Alliez, Joshua A. Levine, Andrei Sharf, and Claudio T. Silva. State of the art in surface reconstruction from point clouds. In *35th Annual Conference of the European Association for Computer Graphics, Eurographics 2014 - State of the Art Reports*. The Eurographics Association, 2014.

[10] Fausto Bernardini, Joshua Mittleman, Holly Rushmeier, Cláudio Silva, and Gabriel Taubin. The ball-pivoting algorithm for surface reconstruction. *IEEE transactions on visualization and computer graphics*, 5(4):349–359, 1999.

[11] Tilak Bhattacharya, Emmanuele DiBenedetto, and Juan Manfredi. Limits as $p \to \infty$ of $\triangle_p u_p = f$ and related external problems. *Rendiconti del Seminario Matematico Università e Politecnico di Torino*, 47:15–68, 1989.

[12] Stephen Boyd, Neal Parikh, Eric Chu, Borja Peleato, Jonathan Eckstein, et al. Distributed optimization and statistical learning via the alternating direction method of multipliers. *Foundations and Trends® in Machine learning*, 3(1):1–122, 2011.

[13] Stephen Boyd and Lieven Vandenberghe. *Convex optimization*. Cambridge University Press, 2004.

[14] Fatih Calakli and Gabriel Taubin. SSD: Smooth signed distance surface reconstruction. In *Computer Graphics Forum*, volume 30, pages 1993–2002. Wiley Online Library, 2011.

[15] Vicent Caselles, Gloria Haro, Guillermo Sapiro, and Joan Verdera. On geometric variational models for inpainting surface holes. *Computer Vision and Image Understanding*, 111(3):351–373, 2008.

[16] Zhiqin Chen and Hao Zhang. Learning implicit fields for generative shape modeling. In *Proceedings of the IEEE/CVF Conference on Computer Vision and Pattern Recognition*, pages 5939–5948, 2019.

[17] Alexander G. Churbanov and Petr N. Vabishchevich. Numerical solution of boundary value problems for the eikonal equation in an anisotropic medium. *Journal of Computational and Applied Mathematics*, 362:55–67, 2019.

[18] Tamal K. Dey, Gang Li, and Jian Sun. Normal estimation for point clouds: A comparison study for a voronoi based method. In *Proceedings Eurographics/IEEE VGTC Symposium Point-Based Graphics*, pages 39–46. IEEE, 2005.

[19] Philipp Erler, Paul Guerrero, Stefan Ohrhallinger, Niloy J Mitra, and Michael Wimmer. Points2surf learning implicit surfaces from point clouds. In *Computer Vision–ECCV 2020: 16th European Conference, Glasgow, UK, August 23–28, 2020, Proceedings, Part V*, pages 108–124. Springer, 2020.

[20] Pierre-Alain Fayolle. Signed distance function computation from an implicit surface. *arXiv preprint arXiv:2104.08057*, 2021.

[21] Henry Fuchs, Zvi M Kedem, and Samuel P Uselton. Optimal surface reconstruction from planar contours. *Communications of the ACM*, 20(10):693–702, 1977.

[22] Tom Goldstein and Stanley Osher. The split Bregman method for L1-regularized problems. *SIAM journal on imaging sciences*, 2(2):323–343, 2009.

[23] Amos Gropp, Lior Yariv, Niv Haim, Matan Atzmon, and Yaron Lipman. Implicit geometric regularization for learning shapes. ICML'20, page 11. JMLR.org, 2020.

[24] Jooyoung Hahn, Karol Mikula, and Peter Frolkovič. Laplacian regularized eikonal equation with Soner boundary condition on polyhedral meshes. *arXiv preprint arXiv:2301.11656*, 2023.

[25] Jooyoung Hahn, Jie Qiu, Eiji Sugisaki, Lei Jia, Xue-Cheng Tai, and Hock Soon Seah. Stroke-based surface reconstruction. *Numerical Mathematics: Theory, Methods and Applications*, 6:297–324, 2013.

[26] Kaiming He, Xiangyu Zhang, Shaoqing Ren, and Jian Sun. Delving deep into rectifiers: Surpassing human-level performance on imagenet classification. In *Proceedings of the IEEE international conference on computer vision*, pages 1026–1034, 2015.

[27] Yuchen He, Sung Ha Kang, and Hao Liu. Curvature regularized surface reconstruction from point clouds. *SIAM Journal on Imaging Sciences*, 13(4):1834–1859, 2020.

[28] Hugues Hoppe, Tony DeRose, Tom Duchamp, John McDonald, and Werner Stuetzle. Surface reconstruction from unorganized points. In *Proceedings of the 19th annual conference on computer graphics and interactive techniques*, pages 71–78, 1992.

[29] Hui Huang, Dan Li, Hao Zhang, Uri Ascher, and Daniel Cohen-Or. Consolidation of unorganized point clouds for surface reconstruction. *ACM transactions on graphics (TOG)*, 28(5):1–7, 2009.

[30] Bernhard Kawohl. On a family of torsional creep problems. *Journal für die reine und angewandte Mathematik*, 410:1–22, 1990.

[31] Michael Kazhdan, Matthew Bolitho, and Hugues Hoppe. Poisson surface reconstruction. In *Proceedings of the fourth Eurographics symposium on Geometry processing*, volume 7, 2006.

[32] Diederik P. Kingma and Jimmy Ba. Adam: A method for stochastic optimization. *arXiv preprint arXiv:1412.6980*, 2014.

[33] Leo Koenigsberger. *Hermann von Helmholtz*. Clarendon pPress, 1906.

[34] Aditi Krishnapriyan, Amir Gholami, Shandian Zhe, Robert Kirby, and Michael W Mahoney. Characterizing possible failure modes in physics-informed neural networks. *Advances in Neural Information Processing Systems*, 34:26548–26560, 2021.

[35] Marc Levoy, Kari Pulli, Brian Curless, Szymon Rusinkiewicz, David Koller, Lucas Pereira, Matt Ginzton, Sean Anderson, James Davis, Jeremy Ginsberg, Jonathan Shade, and Duane Fulk. The digital Michelangelo project: 3D scanning of large statues. In *Proceedings of the 27th Annual Conference on Computer Graphics and Interactive Techniques*, SIGGRAPH ’00, pages 131–144, USA, 2000. ACM Press/Addison-Wesley Publishing Co.

[36] Peter Lindqvist. *Notes on the p-Laplace equation*. Number 161. University of Jyväskylä, 2017.

[37] Yaron Lipman. Phase transitions, distance functions, and implicit neural representations. In *International Conference on Machine Learning*, 2021.

[38] William E. Lorensen and Harvey E. Cline. Marching cubes: A high resolution 3D surface construction algorithm. *ACM SIGGRAPH computer graphics*, 21(4):163–169, 1987.

[39] Baorui Ma, Zhizhong Han, Yu-Shen Liu, and Matthias Zwicker. Neural-Pull: Learning signed distance functions from point clouds by learning to pull space onto surfaces. In *International Conference on Machine Learning*, 2020.

[40] Zoltan Csaba Marton, Radu Bogdan Rusu, and Michael Beetz. On fast surface reconstruction methods for large and noisy point clouds. In *2009 IEEE international conference on robotics and automation*, pages 3218–3223. IEEE, 2009.

[41] Lars Mescheder, Michael Oechsle, Michael Niemeyer, Sebastian Nowozin, and Andreas Geiger. Occupancy networks: Learning 3D reconstruction in function space. In *Proceedings of the IEEE/CVF conference on computer vision and pattern recognition*, pages 4460–4470, 2019.

[42] Mateusz Michalkiewicz, Jhony K Pontes, Dominic Jack, Mahsa Baktashmotlagh, and Anders Eriksson. Deep Level Sets: Implicit surface representations for 3D shape inference. *CoRR*, 2019.

[43] Carsten Moenning and Neil A. Dodgson. Fast marching farthest point sampling for implicit surfaces and point clouds. *Computer Laboratory Technical Report*, 565:1–12, 2003.

[44] Jeong Joon Park, Peter Florence, Julian Straub, Richard Newcombe, and Steven Lovegrove. DeepSDF: Learning continuous signed distance functions for shape representation. In *Proceedings of the IEEE/CVF conference on computer vision and pattern recognition*, pages 165–174, 2019.

[45] Yesom Park, Chang Hoon Song, Jooyoung Hahn, and Myungjoo Kang. ReSDF: Redistancing implicit surfaces using neural networks. *arXiv preprint arXiv:2305.08174*, 2023.

[46] Adam Paszke, Sam Gross, Soumith Chintala, Gregory Chanan, Edward Yang, Zachary DeVito, Zeming Lin, Alban Desmaison, Luca Antiga, and Adam Lerer. Automatic differentiation in pytorch. 2017.

[47] Donald W. Peaceman and Henry H. Rachford, Jr. The numerical solution of parabolic and elliptic differential equations. *Journal of the Society for Industrial and Applied Mathematics*, 3(1):28–41, 1955.

[48] Songyou Peng, Chiyu Jiang, Yiyi Liao, Michael Niemeyer, Marc Pollefeys, and Andreas Geiger. Shape As Points: A differentiable Poisson solver. *Advances in Neural Information Processing Systems*, 34:13032–13044, 2021.

[49] Albert Pumarola, Artsiom Sanakoyeu, Lior Yariv, Ali K. Thabet, and Yaron Lipman. VisCo grids: Surface reconstruction with viscosity and coarea grids. In *NeurIPS*, 2022.

[50] Fu Qiancheng, Xu Qingshan, Ong Yew-Soon, and Tao Wenbing. Geo-Neus: Geometry-consistent neural implicit surfaces learning for multi-view reconstruction. *Advances in Neural Information Processing Systems*, 35:3403–3416, 2022.

[51] Maziar Raissi, Paris Perdikaris, and George E Karniadakis. Physics-informed neural networks: A deep learning framework for solving forward and inverse problems involving nonlinear partial differential equations. *Journal of Computational physics*, 378:686–707, 2019.

[52] Jack Richter-Powell, Yaron Lipman, and Ricky T. Q. Chen. Neural conservation laws: A divergence-free perspective. In *Advances in Neural Information Processing Systems*, 2022.

[53] Liu Shaohui, Zhang Yinda, u Peng Songyo, Shi Boxin, Pollefeys Marc, and Cui. Zhaopeng. DIST: Rendering deep implicit signed distance function with differentiable sphere tracing. *IEEE/CVF Conference on Computer Vision and Pattern Recognition*, pages 2019–2028, 2020.

[54] Vincent Sitzmann, Eric R. Chan, Richard Tucker, Noah Snavely, and Gordon Wetzstein. MetaSDF: Meta-learning signed distance functions. *Advances in Neural Information Processing Systems*, 2020.

[55] Vincent Sitzmann, Julien N. P. Martel, Alexander W. Bergman, David B. Lindell, and Gordon Wetzstein. Implicit neural representations with periodic activation functions. In *Proceedings of the 34th International Conference on Neural Information Processing Systems*, number 626 in NIPS'20, Red Hook, NY, USA, 2020. Curran Associates Inc.

[56] Matthew Tancik, Pratul Srinivasan, Ben Mildenhall, Sara Fridovich-Keil, Nithin Raghavan, Utkarsh Singhal, Ravi Ramamoorthi, Jonathan Barron, and Ren Ng. Fourier features let networks learn high frequency functions in low dimensional domains. *Advances in Neural Information Processing Systems*, 33:7537–7547, 2020.

[57] J. Van Bladel. On Helmholtz's theorem in finite regions. Technical report, CM-P00066539, 1958.

[58] He Wang, Srinath Sridhar, Jingwei Huang, Julien Valentin, Shuran Song, and Leonidas J Guibas. Normalized object coordinate space for category-level 6D object pose and size estimation. In *Proceedings of the IEEE/CVF Conference on Computer Vision and Pattern Recognition*, pages 2642–2651, 2019.

[59] Sifan Wang, Yujun Teng, and Paris Perdikaris. Understanding and mitigating gradient flow pathologies in physics-informed neural networks. *SIAM Journal on Scientific Computing*, 43(5):A3055–A3081, 2021.

[60] Yilun Wang, Junfeng Yang, Wotao Yin, and Yin Zhang. A new alternating minimization algorithm for total variation image reconstruction. *SIAM Journal on Imaging Sciences*, 1(3):248–272, 2008.

[61] Qiangeng Xu, Weiyue Wang, Duygu Ceylan, Radomir Mech, and Ulrich Neumann. DISN: Deep implicit surface network for high-quality single-view 3D reconstruction. *Advances in neural information processing systems*, 32, 2019.

[62] Lior Yariv, Yoni Kasten, Dror Moran, Meirav Galun, Matan Atzmon, Basri Ronen, and Yaron Lipman. Multiview neural surface reconstruction by disentangling geometry and appearance. *Advances in Neural Information Processing Systems*, 33:2492–2502, 2020.

[63] Jingyang Zhang, Yao Yao, Shiwei Li, Tian Fang, David McKinnon, Yanghai Tsin, and Long Quan. Critical regularizations for neural surface reconstruction in the wild. In *Proceedings of the IEEE/CVF Conference on Computer Vision and Pattern Recognition*, pages 6270–6279, 2022.

[64] Hong-Kai Zhao, Stanley Osher, and Ronald Fedkiw. Fast surface reconstruction using the level set method. In *Proceedings IEEE Workshop on Variational and Level Set Methods in Computer Vision*, pages 194–201. IEEE, 2001.

[65] Qingnan Zhou and Alec Jacobson. Thingi10k: A dataset of 10,000 3D-printing models. *arXiv preprint arXiv:1605.04797*, 2016.

A More discussion on curl-free term

This section is devoted to both theoretically and empirically validate the necessity of the curl-free loss term. One might think that the curl-free term is unnecessary, since a curl-free G can be obtained by reducing the L^2 penalty term for the variable splitting constraint $\nabla u = G$. However, this penalty term is not sufficient to train G as a conservative vector field. In subsequent sections, we prove this theoretically and verify experimentally that this is indeed the case in practice.

A.1 Theoretical justification

In the following theorem, we opine that minimizing the L^2 energy of $\|\nabla u - G\|$ in (8) without the curl-free term is not sufficient to obtain a conservative vector field G.

Theorem A.1. *There is a sequence $\{u_n, G_n\}_{n\in\mathbb{N}}$ such that $\int_\Omega \|\nabla u_n - G_n\|^2 \, d\mathbf{x} \to 0$ as $n \to \infty$, but G_n does not converge to a curl-free vector field.*

Proof. For every $\{u_n\}_{n\in\mathbb{N}}$ defined on $\Omega = [0,1]^3$, set

$$G_n(x,y,z) = \nabla u_n(x,y,z) + \left(0, \frac{1}{n}\sin(2\pi n x), 0\right) \in \mathbb{R}^3.$$

Then,

$$\begin{aligned} \int_\Omega \|\nabla u_n - G_n\|^2 \, d\mathbf{x} &= \int_\Omega \left\| \left(0, \frac{1}{n}\sin(2\pi n x), 0\right) \right\|^2 d\mathbf{x} && (14) \\ &= \frac{1}{n^2} \int_\Omega \sin^2(2\pi n x) \, d\mathbf{x} && (15) \\ &\to 0, && (16) \end{aligned}$$

as $n \to \infty$. However,

$$\nabla \times G_n(x,y,z) = (0, 0, \cos(2\pi n x))$$

does not converges to zero. □

Remark A.2. Note that for a G_n set in the proof of the above theorem A.1, $\int_\Omega \|\nabla \times G_n\|^2 \, d\mathbf{x} = \frac{1}{2}$ is a positive constant independent of n. This implies that we can prevent the pathological example above by adding the curl-free loss term. Therefore, the curl-free term is necessary to accurately learn the gradient field G.

A.2 Empirical Validation

To examine the practical effect of the curl-free term on learning a conservative vector field, we include experimental results on a simple example of a sphere of radius 0.5 centered at the origin. Figure 8 depicts the level set contours of the trained u of a cross section cut at the planes $x = 0.2$ and 0.4, along with the vector field of the trained G projected onto this plane together with the gradient field of the true SDF. We note that the p-Poisson equation (1) gives an SDF that is positive on the interior of the surface and negative on the outside, however, the contours depicted in Figures 8 and 9 are of the opposite sign of the trained u. As shown in the Figure 8, the model trained without the curl-free term learns a vector field G that is not curl-free, resulting in G being distinct from the true gradient field. This ultimately impedes u from correctly learning the SDF. On the other hand, it is evident that the model trained with the curl-free term converges fairly close to the true gradient field. This ultimately helps u to accurately learn the SDF.

B Implementation Details

In this section, we provide more details about the implementation for reproducibility. Note that our code is built on top of IGR [2] (MIT License).

[2] https://github.com/amosgropp/IGR

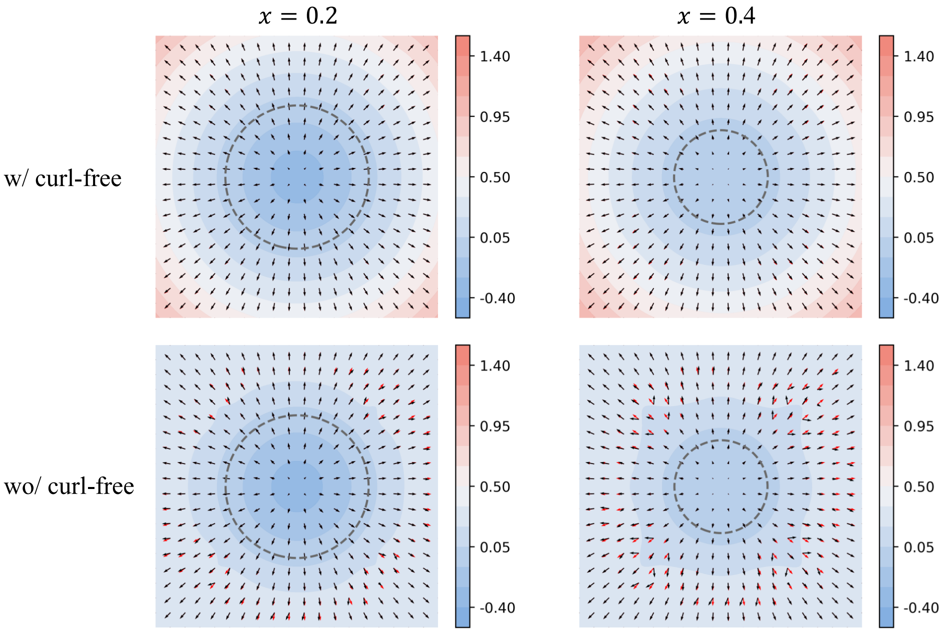

Figure 8: The trained results of a cross section cut in planes $x = 0.2$ (left) and $x = 0.4$ (right). The level-sets show the signed distance fields u learned by the proposed model with (top) and without (bottom) the curl-free term. Dashed contours depict the learned zero level set. Quivers represent the vector field of the trained auxiliary variable G and the true gradient fields are plotted in red arrows.

B.1 Experimental Setup

Parameter Tuning The proposed training loss $\mathcal{L}_{\text{total}}$ (13) is a weighted sum of five loss terms with four regularization parameters $\lambda_1, \lambda_2, \lambda_3$, and λ_4. In all surface reconstruction experiments, we use $\lambda_1 = 0.1,\ \lambda_2 = 0.0001,\ \lambda_3 = 0.0005$, and $\lambda_4 = 0.1$. In the proposed model, p is also a hyperparameter to be chosen. Considering the theoretical fact that p should be infinitely large and numerical simplicity, we set $p = \infty$. We empirically confirm no significant difference between when $p = 100$ and when $p = \infty$. Moreover, we set the smoothing parameter $\epsilon = 1$ for approximating Dirac delta in (13).

Network Architecture As in previous studies [44, 23, 37], we represent the primary and auxiliary outputs by a single 8-layered multi-layer perceptron (MLP) $\mathbb{R}^3 \to \mathbb{R}^7$ with 512 neurons and a skip connection to the fourth layer, but only the output dimension of the last layer is increased by six due to the two auxiliary variables; see Figure 2. We use softplus activation function $\alpha\left(x\right) = \frac{1}{\beta}\ln\left(1 + e^{\beta x}\right)$ with $\beta = 100$. Network weights are initialized by the geometric initialization proposed in [3].

Training details The gradient and the curl of networks are computed with auto-differentiation library (`autograd`) [46]. In all experiments, we use the Adam optimizer [32] with learning rate 10^{-3} decayed by 0.99 every 2,000 iterations. At each iteration, we uniform randomly sample 16,384 points $\mathbf{x} \in \mathcal{X}$ from the point cloud $\mathcal{X}$. We sample the collocation points of Ω as provided in [23]. The collocation points consist of global points and local points. The local collocation points are sampled by perturbing each of the 16,384 points drawn from the point cloud with a zero mean Gaussian distribution with a standard deviation equal to the distance to the 50th nearest neighbor. The global collocation points are made up of approximately 2,000 points from the uniform distribution $U\left(-\eta, \eta\right)$ with $\eta = 1.1$. $F = \frac{1}{3}\mathbf{x}$ is utilized in all experiments.

Baseline models For baseline models on the Thingi10K dataset, we use the official codes of IGR [2] (MIT License), SIREN[3] (MIT License), and DiGS [4] (MIT License). We faithfully follow the official implementation to train each model without normal prior. For the variable splitting representation of the eikonal equation (9), there is a single auxiliary output. Consequently, we use the same 8 layer MLP with 512 nodes, but a network with an output dimension of 4. We normalize the auxiliary output to make it a unit norm, and use the normalized one to represent H.

B.2 Evaluation

Metrics We measure the distance between two point clouds $\mathcal{X}$ and $\mathcal{Y}$ by using the standard one-sided and double-sided ℓ_1 Chamfer distances $d_{\overrightarrow{C}}$, d_C and Hausdorff distances $d_{\overrightarrow{H}}$, d_H. Each are defined as follows:

$$\begin{aligned} d_{\overrightarrow{C}}\left(\mathcal{X},\mathcal{Y}\right) &= \frac{1}{|\mathcal{X}|}\sum_{\mathbf{x}\in\mathcal{X}}\min_{\mathbf{y}\in\mathcal{Y}}\left\|\mathbf{x}-\mathbf{y}\right\|_2, \\ d_C\left(\mathcal{X},\mathcal{Y}\right) &= \frac{1}{2}\left(d_{\overrightarrow{C}}\left(\mathcal{X},\mathcal{Y}\right)+d_{\overrightarrow{C}}\left(\mathcal{Y},\mathcal{X}\right)\right), \\ d_{\overrightarrow{H}}\left(\mathcal{X},\mathcal{Y}\right) &= \max_{\mathbf{x}\in\mathcal{X}}\min_{\mathbf{y}\in\mathcal{Y}}\left\|\mathbf{x}-\mathbf{y}\right\|_2, \\ d_H\left(\mathcal{X},\mathcal{Y}\right) &= \max\left\{d_{\overrightarrow{H}}\left(\mathcal{X},\mathcal{Y}\right)+d_{\overrightarrow{H}}\left(\mathcal{Y},\mathcal{X}\right)\right\}. \end{aligned}$$

When we estimate the distance from a surface, we sample $10M$ uniformly random points from the surface and then measure the distance from the sampled point clouds by the metrics defined above.

Furthermore, in order to measure the accuracy of the trained gradient field, we evaluate Normal Consistency (NC) [41] between the learned G and the surface normal as follows: from given an oriented point cloud $\mathcal{X} = \{\mathbf{x}_i, \mathbf{n}_i\}_{i=1}^N$ comprising of sampled points $\mathbf{x}_i$ and the corresponding outward normal vectors $\mathbf{n}_i$, NC is defined by

$$NC\left(G,\mathbf{n}\right) = \frac{1}{N}\sum_{i=1}^{N}\left|G\left(\mathbf{x}_i\right)^{\mathrm{T}}\mathbf{n}_i\right|, \tag{17}$$

the average of the absolute dot product of the trained G and the surface normals.

Level set extraction We extract the zero level set of a trained neural network u by using the classical marching cubes meshing algorithm [38] on a $512 \times 512 \times 512$ uniform grid.

C Additional Results

C.1 Uniqueness of the solution of p-Poisson equation

In this section, we provide a numerical example supporting the strength of the proposed model regarding the uniqueness of the solution to the p-Poisson equation. The given points are located on a cube centerd at the origin with an edge of the length 1. We consider IGR [23] as an eikonal-rooted baseline, and we train IGR and the proposed PINC with the following three different network initializations: The geometric initialization [23] that IGR originally used and the Kaiming uniform initialization [26] with two different random seeds. The results are summarized in Figure 9. The results show that IGR converges to different solutions depending on the model initializations. In particular, IGR fails to learn the SDF of the cube except for the geometric initialization. On the other hand, the results of PINC with the same initializations show that the proposed model converges to the SDF in all three cases. The numerical results of the chosen example show that the proposed method can pursue the unique solution of the PDE.

C.2 Additional comparison with models utilizing surface normals

In Section 4, we made a comparison with models that do not use the surface normal $\mathbf{n}$ as a supervision. Here, we additionally consider a comparison with models that leverage normal supervision. We

[3] `https://github.com/vsitzmann/siren`

[4] `https://github.com/Chumbyte/DiGS`

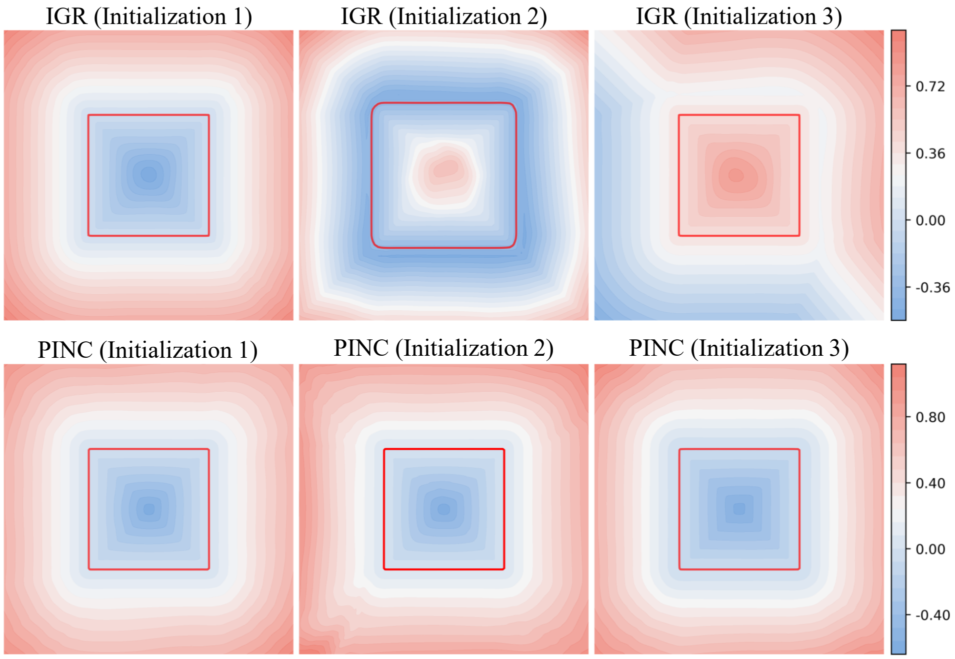

Figure 9: Experimental results show whether a method can find the SDF from different network initializations. IGR and PINC are trained on the synthetic cube data with three network initializations: geometric initialization (initialization 1) and Kaiming initialization with two different random seeds (initializations 2 and 3). Each depicts the trained level-set contours of a cross-section cut in the plane x = 0. Red contours depict the trained zero level set of numerical solutions.

Table 4: Comparison with models that use the surface normal supervision $\mathbf{n}$ on SRB. The proposed model PINC did not utilize the surface normal.

		Anchor				Daratech				DC				Gargoyle				Loard Quas			
		GT		Scans		GT		Scans		GT		Scans		GT		Scans		GT		Scans	
	Model	d_C	d_H	$d_{\vec{C}}$	$d_{\vec{H}}$	d_C	d_H	$d_{\vec{C}}$	$d_{\vec{H}}$	d_C	d_H	$d_{\vec{C}}$	$d_{\vec{H}}$	d_C	d_H	$d_{\vec{C}}$	$d_{\vec{H}}$	d_C	d_H	$d_{\vec{C}}$	$d_{\vec{H}}$
w/$\mathbf{n}$	VisCO	0.21	3.00	0.15	1.07	0.26	4.06	0.14	1.76	0.15	2.22	0.09	2.76	0.17	4.40	0.11	0.96	0.12	1.06	0.7	0.64
	IGR	0.22	4.71	0.12	1.32	0.25	4.01	0.08	1.59	0.17	2.22	0.09	2.61	0.16	3.52	0.06	0.81	0.12	1.17	0.07	0.98
	SAP	0.34	8.83	0.09	2.93	0.22	3.09	0.08	1.66	0.17	3.30	0.04	2.23	0.18	5.54	0.05	1.73	0.13	3.49	0.04	1.17
wo/$\mathbf{n}$	**PINC**	0.29	7.54	0.09	1.20	0.37	7.24	0.11	1.88	0.14	2.56	0.04	2.73	0.16	4.78	0.05	0.80	0.10	0.92	0.04	0.67

consider three baseline models as follows: (i) IGR that evaluates using the surface normal, (ii) VisCo [49], a grid-based method based on the viscosity regularized eikonal equation, and (iii) Shape As Points (SAP) [48], a model that revisits the classical Poisson Surface Reconstruction (PSR) [31] using deep learning. The results are reported in Table 4. We can see that the proposed model performs on par with baselines, despite not utilizing the surface normal. Considering that all of the baselines are PDE-based INR models, the results exhibit the effectiveness of the proposed model (11) in reconstructing a surface from the sole use of raw point clouds.

It is worth note that the proposed model may be interpreted as PSR because of (8). More precisely, the Euler-Lagrange equation of (8) says that the variational problem (8) for finding a scalar function u whose gradient best approximates a given vector field G transforms into the following Poisson problem:

$$\begin{cases} \triangle u = \nabla \cdot G & \text{in } \Omega \\ u = 0 & \text{on } \Gamma. \end{cases} \tag{18}$$

In the conventional PSR, the gradient field is set to surface normals. Thus, the auxiliary variable G can be regarded as playing a role of surface normals for PSR. However, the vector field G in the proposed model is not obtained from the oriented point cloud, but the learnable function that is trained with u at the same time. Moreover, since we bake the p-Poisson equation into G as a hard constraint in (7), we obtain a continuous SDF rather than an indicator function like PSR and SAP. The results confirm that simultaneous training of the gradient field and the SDF, that is, the variable

Table 5: Normal consistency of reconstructed surfaces on SRB.

Model	Anchor	Daratech	DC	Gargoyle	Lord Quas
IGR	0.9706	0.8526	0.9800	0.9765	0.9901
SIREN	0.9438	**0.9682**	0.9735	0.9392	0.9762
DiGS	**0.9767**	0.9680	0.9826	0.9788	0.9907
SAP	0.9750	0.9414	0.9636	0.9731	0.9838
PINC	0.9754	0.9311	**0.9828**	**0.9803**	**0.9915**

Table 6: Normal consistency of reconstructed surfaces on Thingi10K.

Model	Squirrel	Pumpkin	Frogrock	Screstar	Buser head
IGR	**0.9820**	0.9565	0.9509	0.9709	0.9249
SIREN	0.9529	0.8996	0.9035	0.9142	0.8860
DiGS	0.9557	0.9353	0.9468	0.9386	0.9171
SAP	0.9791	0.9520	0.9319	0.9767	0.9004
PINC	0.9816	**0.9583**	**0.9545**	**0.9805**	**0.9376**

splitting method, achieves similar or even better surface restoration than SAP, even without using the given surface normal $\mathbf{n}$.

C.3 Additional quantitative results

We reported Chamfer distances and Hausdorff distances in Tables 1 and 2, but these two metrics do not reflect the complete quality of the restored surface. Here, we evaluate Normal Consistency (NC) (17) which measures how well the model can capture higher order information of the surface. The results on both SRB and Thingi10K datasets are summarized in Tables 5 and 6, respectively. Overall, the proposed model achieves a better NC score than baseline models. In particular, the results show that the proposed model achieves superior NC for the tested examples than SAP, even though it does not employ surface normal supervision.

Moreover, we measure Chamfer distance and Hausdorff distance for ablation studies reported in Figures 6 and 7 of Section 4.3 and summarized them in the Tables 7 and 8, respectively.

More results on effect of p Theoretically, an accurate SDF can be obtained as p grows infinitely. That the same story continues in practice is confirmed by the results shown in Figure 10. We can see that the larger p induces a better reconstruction. This phenomenon is also observed in Figure 7. Moreover, it can be seen that $p = \infty$, which we used in the implementation, gives a similar qualitative result to $p = 100$. These experimental results once again remind us how important it is to be able to use a large p.

Furthermore, we provide numerical verification for the use of $p = \infty$ in Figure 11. For notational convenience, we use the subscript u_p to denote the dependence of the solution on the parameter p. Figure 11 depicts graphs of the mean squared error (MSE) of u_p and u_∞ over different p. MSEs are computed by discretizing the computational domain Ω into a $100 \times 100 \times 100$ uniform grid. The results show that the MSE decreases as p increases. In other words, it confirms that u_p is getting closer to u_∞ as p grows, which supports the justification for using $p = \infty$.

Table 7: Quantitative results on the effect of area loss on daratech.

	GT		Scans	
Model	d_C	d_H	$d_{\vec{C}}$	$d_{\vec{H}}$
PINC wo/ area loss	4.26	53.34	0.20	2.81
PINC w/ area loss	0.37	7.24	0.11	1.88

Table 8: Quantitative results on the ablation study of p.

	Gargoyle				Anchor			
	GT		Scans		GT		Scans	
Model	d_C	d_H	$d_{\overrightarrow{C}}$	$d_{\overrightarrow{H}}$	d_C	d_H	$d_{\overrightarrow{C}}$	$d_{\overrightarrow{H}}$
$p = 2$	3.96	43.13	0.51	6.31	4.32	46.66	0.77	14.58
$p = 10$	0.22	8.14	0.10	1.19	0.50	7.24	0.12	3.02
$p = 100$	0.17	4.90	0.10	0.82	0.31	7.20	0.13	1.80
$p = \infty$	0.16	4.78	0.05	0.80	0.29	7.19	0.11	1.17

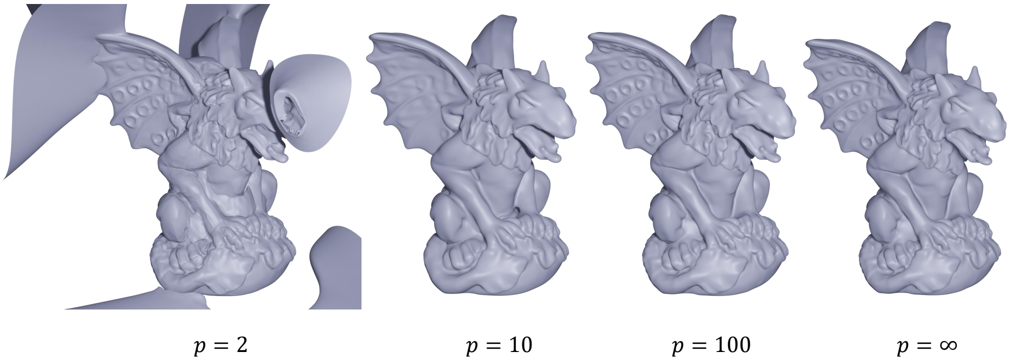

Figure 10: Quality of surface reconstruction with varying p from $p = 2$ to $p = \infty$.

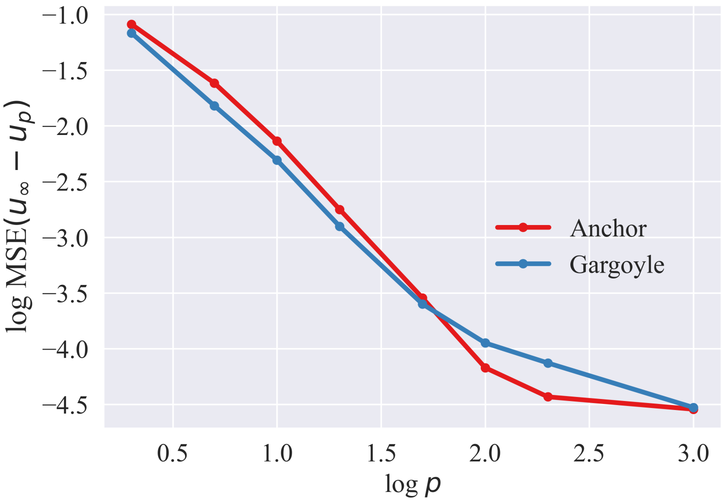

Figure 11: MSEs of u_p and u_∞ over different p.

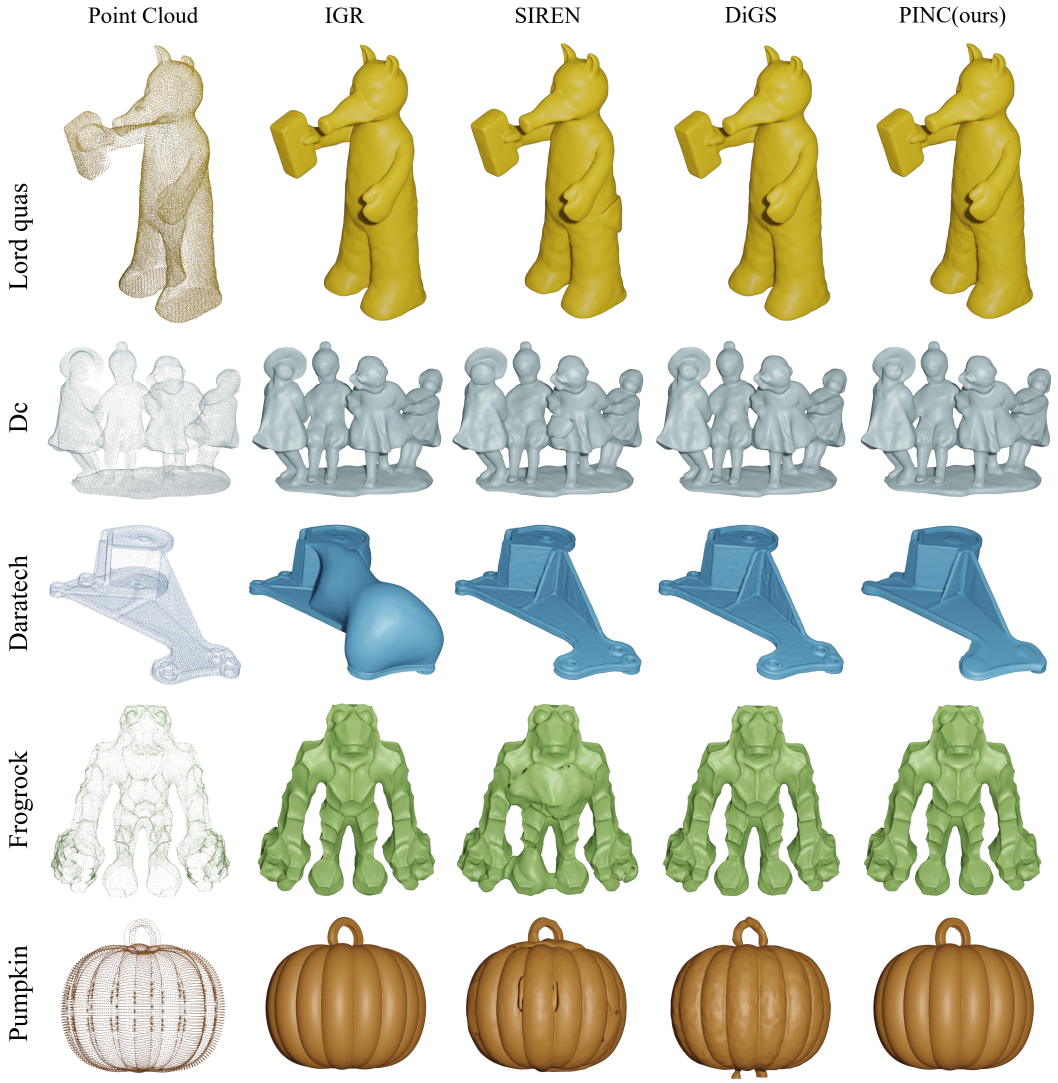

Figure 12: Additional qualitative results of the surface reconstruction on SRB and Thingi10K datasets.

C.4 Additional qualitative results

Figure 12 provides additional qualitative results of surface reconstruction on SRB and Thingi10K discussed in Section 4.1.

Reconstruction of large point clouds We further provide qualitative results for surface reconstruction from large models taken from Thingi10K. The adopted point clouds consist of from 35K to 980K vertices. Figure 13 depicts the qualitative reconstruction results of PINC on these large point clouds. The model is trained with the same configuration used in Section 4.1.

C.5 Training/Inference time

To investigate the computational time of the proposed model, We carefully measured average execution time compared to baselines. In the Table 9, we report the average training time per iteration and inference time at a resolution of 32^3 voxels. The proposed model requires more computational cost than baseline models because of the computation on curl using automatic differentiation.

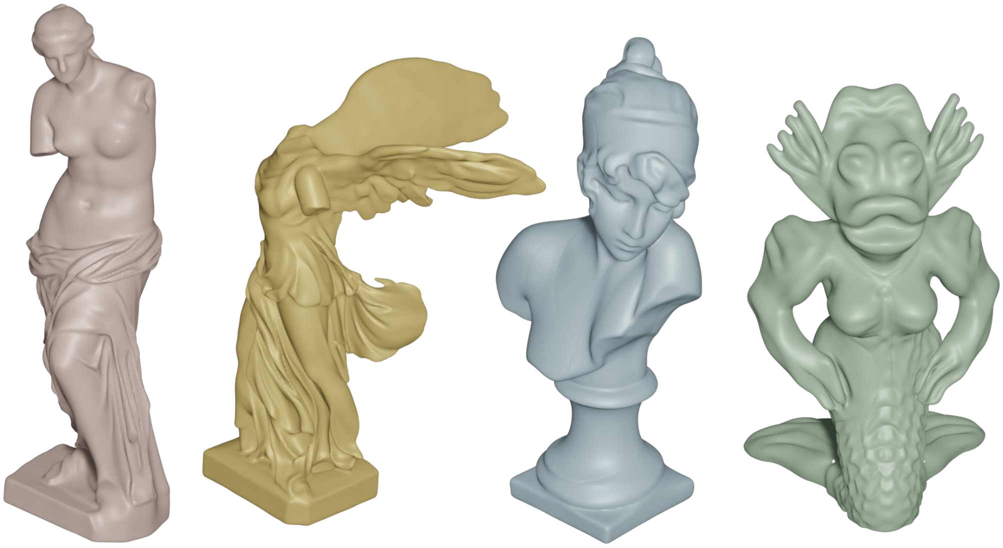

Figure 13: Reconstructed surfaces of large point clouds from Thingi10K.

Table 9: Training and inference times for surface reconstruction on SRB.

Model	IGR	SIREN	DiGS	**PINC**
Training time (ms/iteration)	48.34	13.11	52.34	295.01
Inference time (ms)	6.86	3.51	4.39	6.93